



**HAL**  
open science

## Ceilometer inversion method using water-vapor correction from co-located microwave radiometer

Andres E. Bedoya-Velásquez, Marcos Herreras-Giralda, Roberto Román, Matthias Wiegner, Sidonie Lefebvre, Carlos Toledano, Thierry Huet, Romain Ceolato

► **To cite this version:**

Andres E. Bedoya-Velásquez, Marcos Herreras-Giralda, Roberto Román, Matthias Wiegner, Sidonie Lefebvre, et al.. Ceilometer inversion method using water-vapor correction from co-located microwave radiometer. 2020. hal-02865809v1

**HAL Id: hal-02865809**

**<https://hal.science/hal-02865809v1>**

Preprint submitted on 12 Jun 2020 (v1), last revised 12 Jan 2021 (v2)

**HAL** is a multi-disciplinary open access archive for the deposit and dissemination of scientific research documents, whether they are published or not. The documents may come from teaching and research institutions in France or abroad, or from public or private research centers.

L'archive ouverte pluridisciplinaire **HAL**, est destinée au dépôt et à la diffusion de documents scientifiques de niveau recherche, publiés ou non, émanant des établissements d'enseignement et de recherche français ou étrangers, des laboratoires publics ou privés.

# Ceilometer inversion method using water-vapor correction from co-located microwave radiometer

A. E. Bedoya-Velásquez<sup>1</sup>, M. Herreras-Giralda<sup>2,3</sup>, R. Román<sup>4</sup>, M. Wiegner<sup>5</sup>, S. Lefebvre<sup>6</sup>, C. Toledano<sup>4</sup>, T. Huet<sup>1</sup>, and R. Ceolato<sup>1</sup>

<sup>1</sup>The French Aeospace Lab, ONERA, Toulouse, France

<sup>2</sup>GRASP-SAS, Remote sensing developments, Université des Sciences et Technologies de Lille, Villeneuve d'Ascq, France

<sup>3</sup>Laboratoire d'Optique Atmosphérique, Université des Sciences et Technologies de Lille, Villeneuve d'Ascq, France

<sup>4</sup>Grupo de óptica atmosférica, Universidad de Valladolid, Valladolid, Spain

<sup>5</sup>Meteorologisches Institut, Ludwig-Maximilians-Universität, Theresienstraße 37, 80333 München, Germany

<sup>6</sup>The French Aeospace Lab, ONERA, Palaiseau, France

**Correspondence:** Romain Ceolato (romain.ceolato@onera.fr)

**Abstract.** Ceilometers are widely spread instruments mainly used for cloud base height determination. However, recent models are more sensitive to aerosols; hence, nowadays there is an increasing interest in these instruments to retrieve aerosol optical and microphysical properties. The high number of them distributed around the globe compared to the robust lidar systems and the fact that ceilometers work under unattended conditions are the main reasons behind this interest. In this paper a new methodology is proposed to retrieve aerosol vertical extinction and backscatter profiles from a Vaisala ceilometer CL51 model. This methodology is based in two parts: first, a signal pre-processing with a suppression of the dark current and background noises, and a correction of the water vapor absorption using near-real-time temperature and absolute humidity (AH) profiles from a co-located Microwave radiometer (MWR). Then an iterative Klett-based algorithm that uses AERONET (AEROSOL ROBOTIC NETWORK) AOD (Aerosol Optical Depth) as input is applied to retrieve the extinction and backscatter profiles. The sensitivity of the aerosol retrievals to the use of modelled temperature and absolute humidity from HYSPLIT to correct water vapor absorption, instead of MWR measurements, is studied. The absolute errors found in temperature and AH leads to errors in the pre-processed RCS signals up to 9 %, and then in particle backscatter ( $\beta_p$ ) and particle extinction ( $\alpha_p$ ) coefficients up to 2.2 % and 25 %, respectively.

*Copyright statement.* TEXT

## 15 1 Introduction

Atmospheric aerosols play a crucial role in atmospheric dynamics and the energy balance of the Earth. The main impact of the aerosols related-interactions are: (i) the aerosol-radiation interaction (ARI), affecting the radiative fluxes of the Earth by absorbing and scattering solar and thermal radiation, and (ii) aerosol-cloud interaction (ACI) which are mainly associated to

the modification of cloud properties and precipitation caused by aerosols (Boucher et al., 2013).

During the last decades, different active and passive remote sensors in synergistic operation have become a powerful strategy for the better determination of the atmospheric aerosol properties (optical and microphysical). Previous works have shown that synergy between active remote sensors as lidar systems (light detection and ranging) and passive remote sensors, e.g. sunphotometers or microwave radiometer (MWR), allows to obtain advanced and vertically resolved aerosol properties (Chaikovsky et al., 2016; Lopatin et al., 2013; Benavent-Oltra et al., 2017; Benavent-Oltra et al., 2019) and to study phenomena like aerosol hygroscopic growth (Bedoya-Velásquez et al., 2018) and the aerosol vertical dynamics using as proxy the planetary boundary layer (PBL) height (de Arruda Moreira et al., 2019). The main drawbacks of these synergies are the cost of having the instrumentation operating together and also that most of the instruments are semi-automatic, which means that qualified human operation is frequently needed.

Ceilometers are low power single-wavelength lidar-based instruments which operate automatically, unattended and continuously. These instruments are commonly used for cloud base height determination and PBL studies, but recent ceilometer models have become a useful alternative to lidars for aerosol studies where lidar instruments are not available. These systems have been widely spread along the world with more than 1000 ceilometers installed over Europe, Asia and America. Currently, the COST Action ES1303 TOPROF (TOwards operational ground based PROFiling with ceilometers, doppler lidars and microwave radiometers for improving weather forecasts) has dedicated part of their interests on working in a better characterization of the ceilometer products and related uncertainties, and also E-PROFILE, a program of EUMETNET (EUropean METeorological services NETwork), is focused on the harmonization of ceilometer measurements and data provision across Europe, meaning that the interest in quantitative aerosol products from these instruments is increasing. In the last decade, ceilometers started to be used for long term studies of phenomena less investigated with remote sensors like aerosol hygroscopic growth (Bedoya-Velásquez et al., 2019), to improve the forecasting models for example to predict fog events (Haeffelin et al., 2016), to retrieve profiles of aerosol properties (Wiegner et al., 2014; Jin et al., 2015; Cazorla et al., 2017; Román et al., 2018) and to characterize them (Herrerias et al., 2018 and Titos et al., 2019).

CHM15k ceilometer model (Lufft manufacturer) is widely used for aerosol inversion, mainly because it operates with a similar configuration as the commercial lidar systems, therefore the signals quality has been deeply studied and their capabilities are well known. Other ceilometers used for the same end are the CL31 and CL51 models (Vaisala Inc.), but as it was shown in Kotthaus et al., 2016, depending of the firmware and other features, Vaisala ceilometers present lots of drawbacks such as non-expected signal shapes and high electronic noises. In Marcos et al., 2018 is presented a new type of correction that improves the signal shape, named dark signal removal, making a substitution of the dark current measurements. In addition, as the emission line of the Vaisala CL-51 ceilometer is centered around 910 nm, water vapor absorption plays a critical role affecting the quality of the signal. Wiegner and Gasteiger, 2015 describe a methodology to make a water vapor correction of the signal using modelled water vapor absorption cross section and radiosondes for retrieving aerosol properties. After considering all

this pre-processing, it is possible to use the ceilometer signal for aerosol retrieval using traditional methods such as the Klett algorithm (Klett, 1985; Cazorla et al., 2017).

In this framework, the main objective of this work is to present a new methodology, based on a modified Klett algorithm  
5 Cazorla et al., 2017, to retrieve optical aerosol properties from Vaisala CL51 ceilometers. To this end, a data pre-processing  
is required, including the suppression of the dark current (DC), height-dependant background (BG) noises, and water vapor  
correction in near-real time by using a co-located microwave radiometer (MWR). The methodology allows to determine the  
error propagation when modelled atmospheric profiles are used for aerosol inversion products instead of using co-located mea-  
surements.

10

The manuscript is organized as follows. The site, instrumentation and data used are presented in Section 2, while Section  
3 explain the applied methodology in terms of the signal pre-processing. Section 4 describes the Klett method to retrieve the  
aerosol profiles, and Section 5 shows the uncertainty in the retrievals caused by the use of water vapor derived from modelled  
radiosoundings instead of MWR data. Finally, Section 6 summarizes the main conclusions.

## 15 **2 Site, Instrumentation and data availability**

### **2.1 ONERA site**

ONERA, the French Aerospace Lab, is a research institute located in Toulouse, Occitanie, in the southern part of France (N:  
43° 34' 12", E: 1° 28' 24"). The mission of the Optics and Associated Techniques Department (DOTA) is to conduct studies and  
research in Optronics. These studies are conducted primarily for the benefit of the fields of Aeronautics, Space and Defence, but  
20 also for other fields such as security, environment, astronomy and medical imaging. MELOPEE Lab is a light-scattering lidar  
laboratory dedicated to the development of active remote-sensing instrument for light-scattering investigations. For this work,  
a ceilometer and a ground-based microwaver radiometer located on roof-top of the building were used for this experiment.  
Toulouse is a region with a humid subtropical climate dominated by Autan wind, which is a south-easterly wind from the  
Mediterranean. Due to the Garone river that divides the city between east and west crossing it from south to north, Toulouse  
25 presents rather high relative humidity (around 80%) almost all over the year. The seasonal behaviour drives to have hot summers  
and cold winters.

### **2.2 Vaisala CL51 ceilometer**

A CL51 Vaisala ceilometer, located at the ONERA site, have been used in this work. This is an active remote sensor that con-  
tinuously operates (24/7) emitting pulsed laser radiation towards the atmosphere centered at  $910 \pm 10$  nm. The backscattered  
30 radiation by the atmosphere is collected by a telescope in coaxial configuration, reducing the overlap height; the full overlap  
can be reached below 250 m agl according to the manufacturer specifications. The detection system is based on an APD de-

tor. The backscattered signal from the atmosphere is measured with spatial and temporal resolutions up to 10 m and 15 s respectively. More technical information can be found in Kotthaus et al., 2016. The spectral range of the emitted and received light by the instrument is affected by atmospheric water vapor absorption, which has a direct a direct impact on the recorded attenuated backscatter profile, which is the main product of the instrument.

5

Ceilometer records are based on the elastic lidar equation considered under single scattering approximation as follows:

$$RCS(R) = KO(R)\beta(R)T^2(R) \quad (1)$$

where  $RCS(R)$  is the range corrected signal (the recorded signal divided by the square of range);  $K$  is a constant that involves system characteristics (optics and electronics);  $O(R)$  is the overlap function referring to the geometrical probability of fully signal collection as a function of height;  $\beta$  is the backscatter coefficient and  $T^2$  is the atmospheric transmittance. The double pathway transmittance is defined as:

$$T^2(R) = \exp \left[ -2 \int_0^R \alpha(r) dr \right] \quad (2)$$

where  $\alpha$  is the atmospheric extinction coefficient. In a general formulation,  $\beta$  and  $\alpha$  takes into account the contribution of the particles and molecules in the atmosphere, therefore assuming that  $K$  and  $O(R)$  are well known, and considering Eq.2, lidar equation can be rewritten as follows:

$$\frac{RCS(R)}{KO(R)} = U(R) = \beta(R) \exp \left[ -2 \int_0^R \alpha(r) dr \right] \quad (3)$$

The  $U(R)$  term is the main product retrieved from ceilometers, but in practice this coefficient cannot be always determined because  $K$  and  $O(R)$  parameters are unknown most of the time. Due to this elastic lidar formulation, the wavelength dependency is omitted from the equations. The analytical solution of the Eq.3 can be obtained by using Klett-Fernald method (Klett, 1981; Klett, 1985) assuming a constant extinction-to-backscatter ratio, also known as lidar ratio ( $LR$ ). Other atmospheric parameters are involved in the solution of the lidar equation, but those will be discussed in further sections. The data used in this work were measured continuously from October to November 2019 with temporal resolution about 36 s/profile and vertical resolution of 10 m (from 10 m to 15400 km agl). The instrument records 2400 measures per day of RCS profiles, but it also provides cloud base height, and other metadata.

### 25 2.3 RPG-HATPRO MWR

A ground-based microwave radiometer (RPG-HATPRO, Radiometer physics GmbH) is co-located to the mentioned ceilometer. MWR is considered as a passive remote sensor that performs measures unattended of the brightness temperatures of oxygen

and water vapor in the atmosphere. The oxygen is measured in the K-band (51-58 GHz) and the water vapor in the V-band from 22 to 31 GHz with a radiometric resolution between 0.3 and 0.4 rms errors at 1.0 s integration time.

A previously trained neural network algorithm (Rose et al., 2005) is used to retrieve temperature and relative humidity (RH) and absolute humidity (AH) profiles. The temperature and RH profiles are provided at 92 height bins with variable vertical resolution and covering the first 10 km of the atmosphere. Temperature and RH profiles performance (accuracy and precision) has been studied in previous studies using radiosondes as references and finding that the temperature accuracy and precision is up to  $1 \pm 1.1$  K and close to  $6 \pm 8$  % for RH under cloud-free conditions Bedoya-Velásquez et al., 2019; this pointed out the potential of these systems to retrieving atmospheric variables. Regarding the data availability for this study, the MWR provides up to 600 temperature, relative humidity and absolute humidity profiles per day with temporal resolution up to 2 min/profile. Temperature profiles had a composite format that combined the high spatial resolution of the atmospheric boundary layer profiles product with the standard temperature profiles.

## 2.4 CIMEL sun/sky photometer

A sun/sky photometer CIMEL CE318-N (Cimel Electronique S.A.S.)(Holben et al., 1998) is operating since 2013 at the south-east part of Toulouse (43.57 N, 1.37 E, at 160 m asl), up to 8 km away from the ceilometer in straight line. This instrument provides automatic measurements of sun and sky radiation at several wavelengths (340, 380, 440, 500, 675, 870, 940, 1020 and 1640 nm). These measurements are processed by AERONET in order to derive the optical and microphysical aerosol properties integrated in column Holben et al., 1998. The main AERONET product is the spectral aerosol optical depth ( $AOD_\lambda$ ). In addition, the channel of 940 nm is used for retrieving the total column water vapor (or precipitable water vapor). AERONET also uses  $AOD_\lambda$  and almucantar sky radiance measurements to retrieve and provide additional aerosol properties including volume size distribution, complex refraction index, and single scattering albedo at various wavelengths (Dubovik and King, 2000; Dubovik et al., 2002; Dubovik et al., 2006). In this work, the AERONET AOD data used is the AERONET level 1.5 (cloud-screened) from AERONET version 3 (Giles et al., 2019), with an uncertainty lower than  $\pm 0.01$  for the wavelengths larger than 440 nm and below 0.02 for shorter wavelengths.

## 2.5 Hysplit GDAS meteorological data base

As a result of the computer analysis and forecast calculation performed at the centers for Environmental prediction (NCEP), it is possible to use an operational system so called Global Assimilation Data System (GDAS) for running the Hybrid Single Particle Lagrangian Integrated Trajectory Model (HYSPLIT)(Stein et al., 2015). One of the HYSPLIT modules allows to retrieve modelled radiosondes with different spatial and temporal resolutions. In this work, we have retrieved HYSPLIT profiles of temperature, relative humidity and pressure for ONERA location with spatial resolution of  $0.5^\circ$  and 3 h of temporal resolution. The total database of radiosoundings used for this study is 488 profiles (October and November 2019) from 0 to 10 km.

### 3 Signal pre-processing

The methodology developed in this paper involves the following 2 stages (Fig.1): (i) the signal pre-processing: contain dark current (DC), background (BG) and water vapor correction by using real co-located atmospheric measurements and (ii) refers to the semi-automatic Klett algorithm.

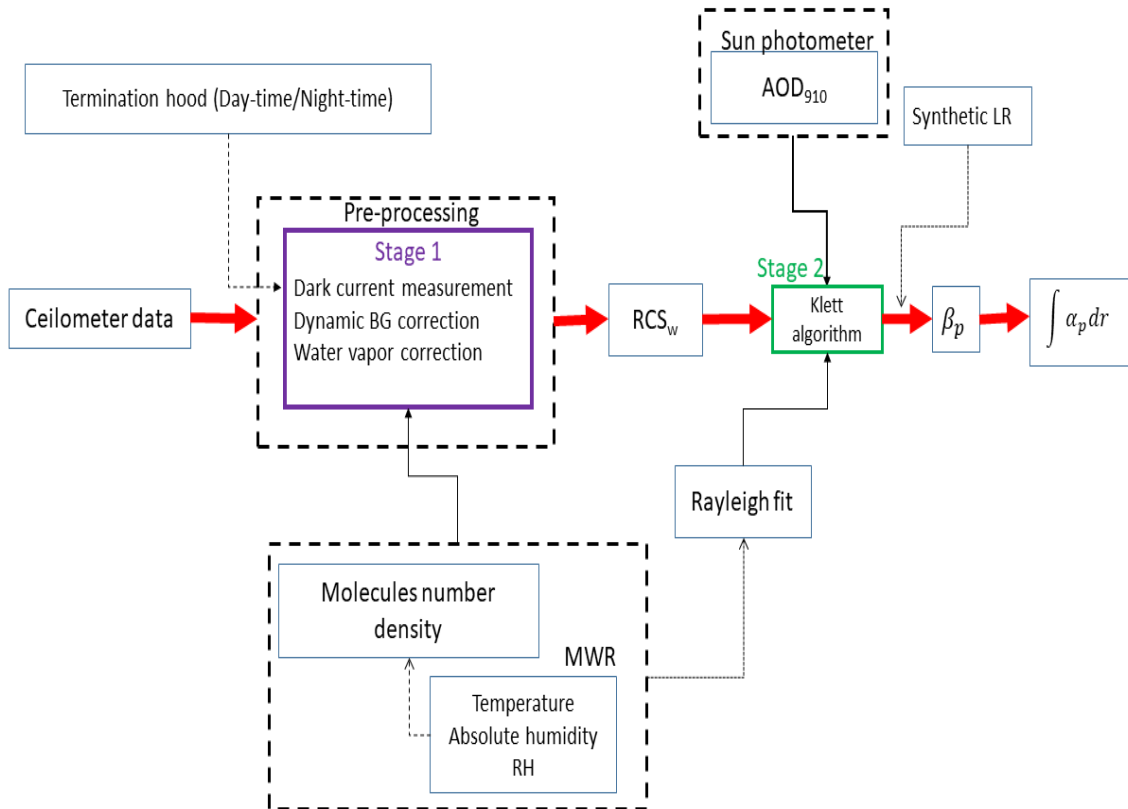


**Figure 1.** Block diagram of the methodology

#### 5 3.1 Dark current correction

First, a ceilometer data pre-processing is performed. For signal noise correction, two types of signal are taken into account. The first one is linked with the electrical noise of the detectors which is so called dark current (DC). In this work, DC measurements were carried out under day-time and night-time conditions using the termination hood accessory delivered with the ceilometer shipping for covering the instrument to avoid external light contamination. The DC was regularly measured twice per week during two weeks, taking samples of 30 minutes at day and night time. During the analyzed period (October-November 2019)

DC does not show a high variability between days, therefore we focused our attention on the day-time and night-time analysis. As example, Fig.2a presents the day-time and night-time mean DC profiles measured from 0.010 km to 15.4 km agl for the 11<sup>th</sup> October 2019. The bias between the profiles (not shown) in the first kilometers (from ground to 1 km agl) is close to zero, but it increased rapidly with height: bias from 1 to 2 km agl increased from 2.5 to 5.0 a.u, from 2 to 6 km agl increased from 5 to 25 a.u and above this height the bias reached up values above 300 a.u. The shape of the DC signal is relatively well balance between negative and positive values around zero until 9 km agl, but above this height the signal is fluctuating strongly describing like a S-shape. From 9 to 11 km agl is seen a positive curve, then the signal decrease from 11 to 14 km agl describing a negative curve for finally increase again from 14 km to the end of the profile. Once the DC is characterized, it must be directly subtracted from the range corrected ceilometer raw data.

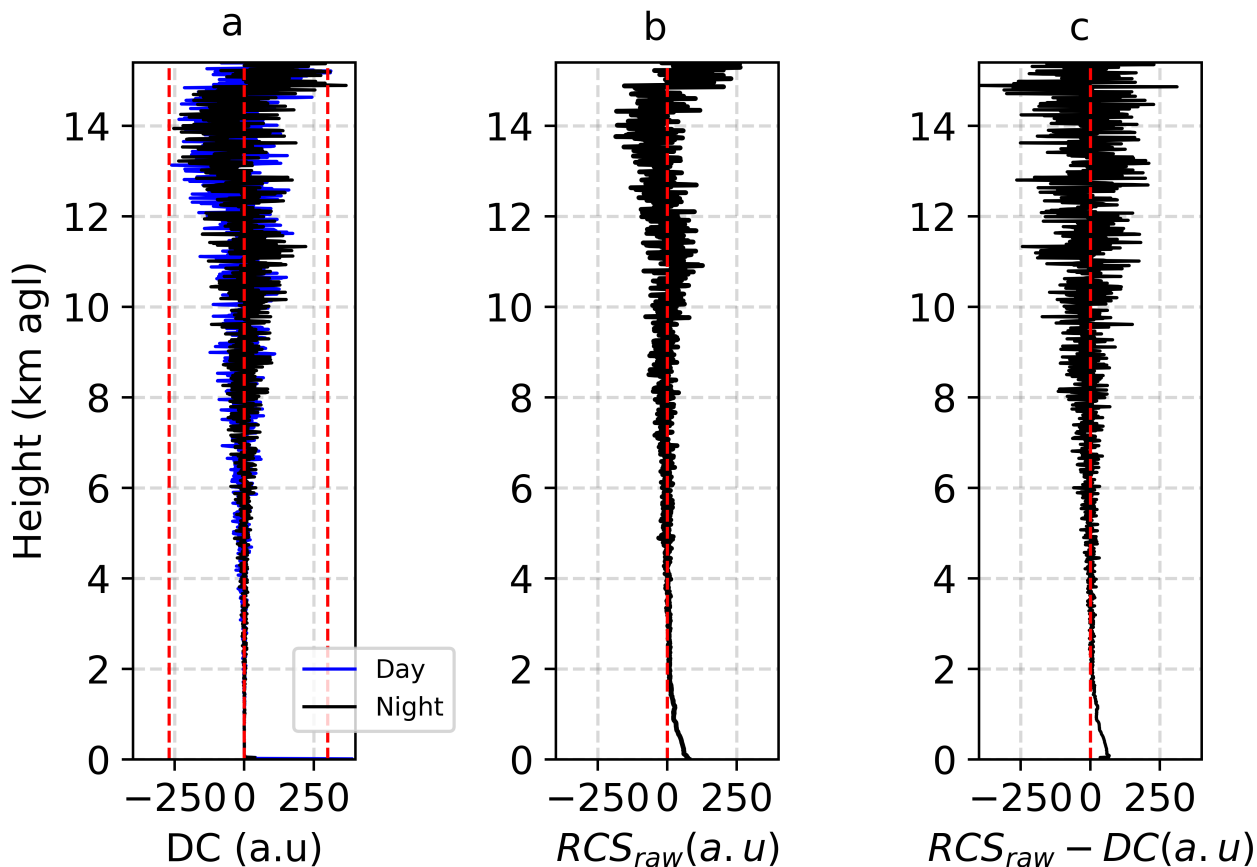


**Figure 2.** Example case corresponding to 11<sup>th</sup> October 2019 of the signals used to calculate the ceilometer signal pre-processing. a) The DC measurements (black: night-time, blue: day-time), and the red dotted lines around  $\pm 250$  are highlighting the maximum noise levels of the signal, b) the  $RCS_{raw}$  signal 1h-averaged around the DC profile, and c) the  $RCS_{raw}$  DC corrected



According to Kotthaus et al., 2016 results, this behavior can be expected for Vaisala ceilometers, however this analysis let us determine the impact that DC measurements have on the  $RCS_{raw}$  signal, evidencing that this instrument is highly noisy above 4 km agl, which was checked for the raw signal and range corrected. The  $RCS_{raw}$  signal shown in Fig.2b was 1h-averaged in order to minimize spatial fluctuations. Testing with the  $RCS_{raw}$ , it was possible to determine that the  $RCS_{raw}$  and DC keeps the same shape in the last kilometers, which give us the possibility to suppressing this fluctuations with continuous DC measurements, and also to define the regions for suppressing the environment-light noise, so called BG accurately.

The DC correction presented in Fig.2c was performed firstly to remove the S-shape fluctuation of the signal and secondly to reduce/suppress some near-range electronic fluctuations. After DC correction, it can be noticed that the signal( $RCS_{cor}^{DC}$ ) is noise cleaned up to 4 km agl, and the S-shape oscillation of the  $RCS_{raw}$  has been suppressed. This S-shape of the Vaisala ceilometer signal is related to the opto-electronic system noises, but this analysis is beyond of the scope in this work.

### 3.2 Background noise

The second noise evaluated during the data pre-processing is the environmental light contamination of the ceilometer signal, which interact such as bias or also know as background (BG) noise. This calculation is performed after DC correction in order to have a signal without electronic fluctuations. For BG correction, first the BG is calculated at 4 different ranges, assumed as molecular, as the mean value of the signal in these ranges: BG1 (7-9 km agl), BG2 (9-11 km agl), BG3 (11-13 km agl) and BG4 (13-15.4 km agl). These ranges are considered because of the BG fluctuations above 7 km evidenced in the standard deviation of the mean value. This procedure provided four possible values to correct the signal, therefore we systematically selected only the scalar BG value that maintained RCS positive below 5 km agl with the lowest standard deviation.

As it is widely known, the signal retrieved from the Vaisala ceilometers presents a challenge to be pre-processed in order to retrieve aerosol optical properties. One of the main challenges is presented in Kotthaus et al., 2016, where was showed that most of Vaisala systems have a positive or negative signal distortion associated to electronic noise fluctuations. The correction of this fluctuation is tackled by suppressing cosmetic offsets (Kotthaus et al., 2016) or dark corrections (Marcos et al., 2018). In this work, the DC measurement and also the search of the best BG value assure that signal noise level and shape is corrected. The corrected signal is defined in the manuscript as follows

$$RCS^*(R) = RCS_{raw} - [DC + BG] \quad (4)$$

where  $RCS_{raw}$  is the raw range corrected signal, DC is a 30 min averaged profile and BG is the mean value that fulfilled the criteria already explained.

In Fig.3 is presented this signal pre-processing, showing that good BG selection is not a trivial process for ceilometers, the best BG range must avoid that  $RCS^*$  became negative rapidly. The example case shows that using BG4 (blue line) instead

BG2 (orange line) leads the  $RCS^*$  signal to be positive above 6 km agl (see the blue line, Fig.3b), but the other BG corrections were driving the  $RCS^*$  to be negative faster, like BG2 (orange signal, Fig.3b).

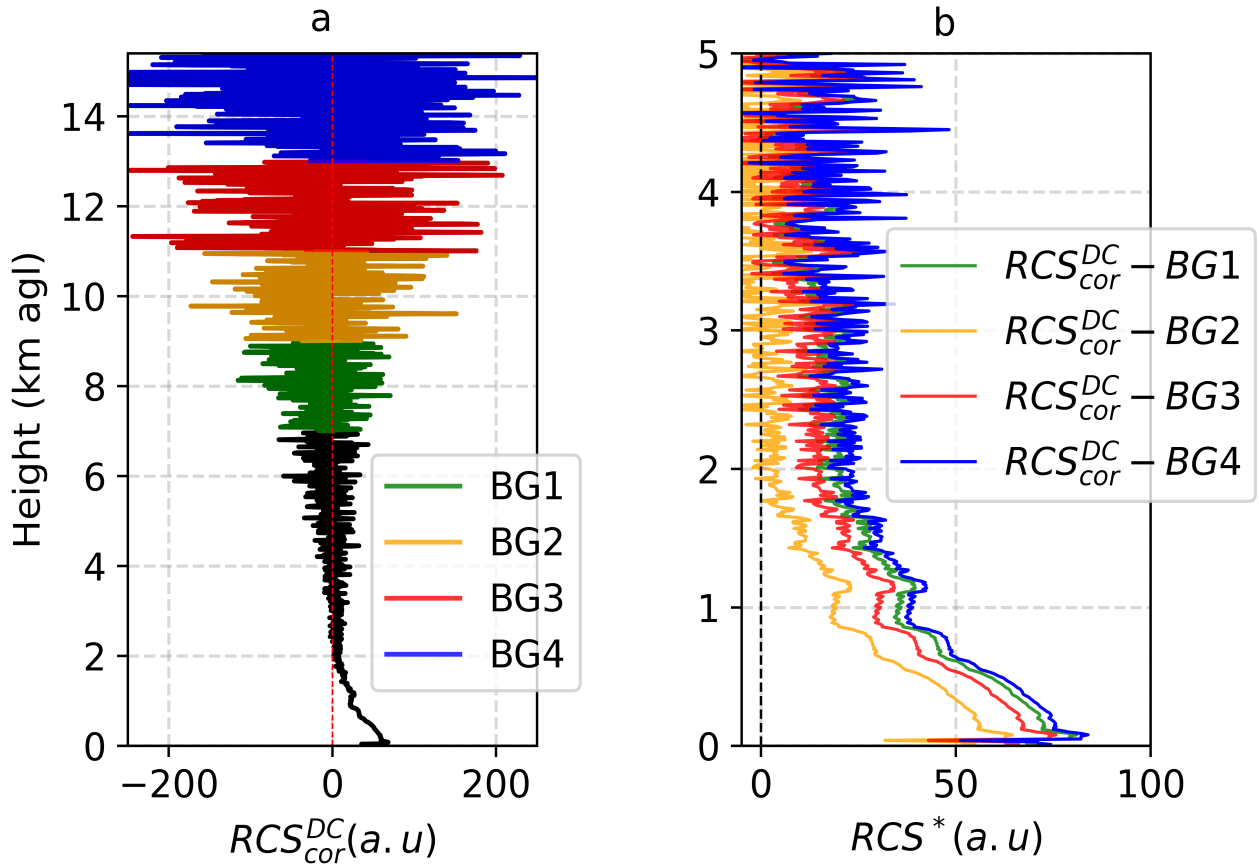


**Figure 3.** The figure presents the BG noise pre-processing applied to the  $RCS_{cor}^{DC}$ . a) Presents the  $RCS_{cor}^{DC}$  signal highlighting the four ranges selected to study of the BG noise. In green line is related to the correction for BG1, orange to BG2, red to BG3 and blue to BG4, b) is the  $RCS^* = RCS_{cor}^{DC} - BG$  signal zoomed until 5 km agl where each color refers to the already mentioned BG ranges.

### 3.3 Water vapor correction

As mentioned before, one of the CL51 drawbacks is the impact of the water vapor absorption on the laser emission line, but previous works demonstrated that this effect can be minimized. The water vapor correction method used in this paper is based on the proposal by Wiegner and Gasteiger, 2015. To perform this correction, absolute humidity and temperature profiles are used as input. In this paper these profiles are from co-located MWR obtained each 2 min from 0 to 10 km agl. These profiles are interpolated to the ceilometer vertical resolution. In order to evaluate coincident measurements, the temporal resolution of

the ceilometer has been reduced to the MWR resolution.

For the water vapor correction it is necessary to rewrite Eq.1, splitting the transmittance term into the contributions of the molecules, particles and water vapor ( $T_m^2$ ,  $T_p^2$ ,  $T_w^2$ ). In this work, the transmittance term for molecules is calculated by using Rayleigh theory fed with real atmospheric measurements (pressure, temperature and RH) from the MWR and the transmittance from particles can be determined as a results of the crosschecking procedure during the Klett inversion explained below.  $T_w^2$  can be defined as:

$$T_w^2 = \exp \left[ -2 \int_0^R \alpha(r)_w dr \right] \quad (5)$$

Where  $\alpha(r)_w = \sigma(r)_w N(r)_w$ , with  $N(r)_w$  the water vapor number concentration and  $\sigma(r)_w$  absorption cross section at the emitted wavelength. The  $N(r)_w$  will be retrieved from atmospheric measurements of absolute humidity profiles like  $N(r)_w = 7.25 \times 10^{22} \text{ AH } R_w$ , where  $R_w = 0.462 \text{ Jg}^{-1} \text{ K}^{-1}$ .  $\sigma(r)_w$  is calculated following the results presented on Wiegner and Gasteiger, 2015 for the absorption cross section simulated profiles. In this context, we assume a Gaussian shape of the ceilometer emission spectrum centered at 910 nm with  $\Delta\lambda = 3.5 \text{ nm}$  (Wiegner and Gasteiger, 2015). As water vapor decrease with height, the Eq.5 is solved for the first 10 km of the atmosphere, but results are only shown until 5 km agl. The water vapor corrected profile is named hereafter as  $RCS_w = RCS^*(R) * T_w^2$ .

Figure4 shows an example case where the water vapor correction is applied following the explained procedure. The atmospheric transmittance due to water vapor molecules is calculated using the profiles of temperature and AH from MWR. Temperature and AH profiles allows us to calculate  $n_w$  until 10 km agl, but the attention is dominating in the first 5 km agl where these variables present a strong-height dependency in the atmosphere (Fig.4a). In the example case shown in Fig.4b (red line), it is possible to evaluate the bias between  $RCS^*$  and  $RCS_w$ , meaning that ceilometer signal tends to be overestimated if water vapor correction is not applied (Fig.4b, gray line). The larger differences between water vapor corrected and no-corrected profiles are within the the first 1.5 km agl meanly because i) tropospheric water vapor molecules are more abundant in this altitudes, and ii) the MWR spatial resolution is better until 2 km agl. This increase of the overestimation is seen on the bias plot (Fig.4c), reaching almost 4 (a.u), but above 1.8 km agl the bias profile tends to be highly noisy. This noise is mainly caused by the increasing of the  $RCS^*$  noise already discussed, and because of the greater uncertainties due to the water vapor transmittance height-dependency.

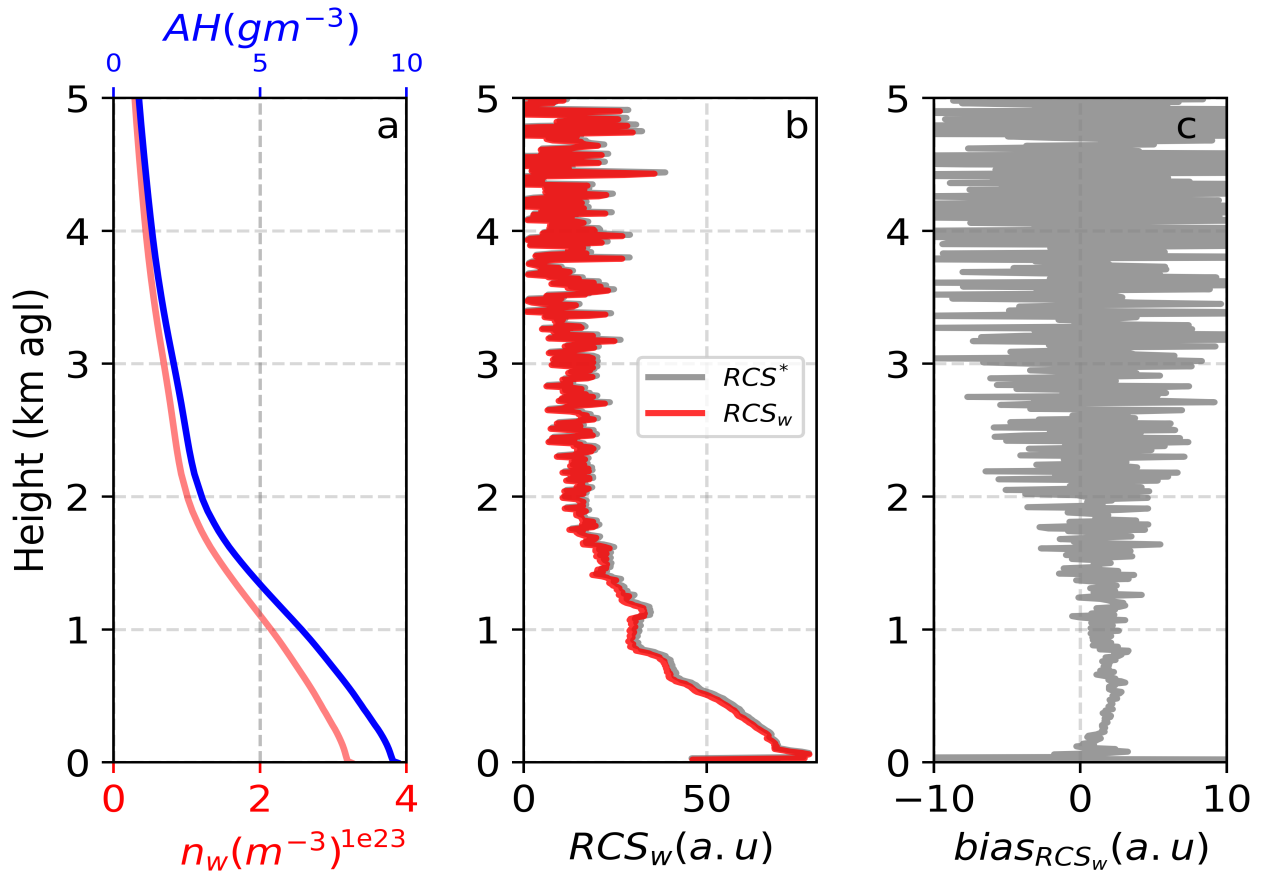


**Figure 4.** Water vapor correction corresponding to 11<sup>th</sup> October 2019 at 06:00 UTC. a) Water vapor number of concentration (red line) and in blue line is represented the AH, b)  $RCS_w$  with/without water vapor correction, red and gray line respectively are shown, and c) is the bias between  $RCS^*$  and  $RCS_w$

#### 4 Retrieval of aerosol profiles

Ceilometer inversions have been successfully proved in Vaisala ceilometers in previous works (Marcos et al., 2018; Wiegner and Gasteiger, 2015). The main challenge is the use of ancillary information from models for either correcting the signal and then invert it. In this work, we propose an approach to tackle this problem by combining co-located atmospheric profiles measured next to the ceilometer and then applying a modified methodology of the semi-automatic lidar Klett inversion proposed in Cazorla et al., 2017.

The aerosol retrieval starts from the following lidar equation

$$RCS_w(R) = C\beta(R)T_m^2T_p^2 \quad (6)$$

Then the backward Klett equation can be expressed as follows,

$$\beta_p = \frac{A_1(R)}{A_2(R)} - \beta_m(R) \quad (7)$$

5 where

$$A_1(R) = RCS_w(R) \exp \left[ 2 \int_r^{r_{ref}} (LR_p - LR_m) \beta_m dr \right] \quad (8)$$

and

$$A_2(R) = \frac{RCS_w(R)}{\beta(r_{ref})_m + \beta(r_{ref})_p} + 2 \int_r^{r_{ref}} LR(r)_p A_1(r) dr \quad (9)$$

where  $\beta_m$  is determined from Rayleigh theory using real atmospheric profiles as inputs and molecular lidar ratio ( $LR_m$ ) is well known from theory. The other terms like particle lidar ratio ( $LR_p$ ), and the reference height ( $r_{ref}$ ) are calculated during the different steps in the implementation of the modified Cazorla et al., 2017 algorithm to Vaisala ceilometer. The Klett inversion has been divided in 3-step process as follows:

- Signal smoothing (Step 1): First the signal is noise-cleaned applying a 1h average to the analyzed profiles. Then, in order to remove some remaining electronic noise, a vertical filter (40 m moving average filter) is applied. The aim of doing this filtering is to clean the  $RCS_w$  of spatial random noises, but preserving the original spatial resolution of the profile.
- Rayleigh fit (Step 2): we compare the  $RCS_w$  with the  $\beta_m$  looking for the Rayleigh zone. The signals are normalized in order to have comparable magnitudes between profiles. After this normalization it is possible to check automatically the region where both signals have similar vertical slopes by means of a linear fitting (from 2 to 5 km agl). The thresholds to consider that both slopes are close enough are up to  $r^2 > 0.7$  for the linear fit of the ceilometer normalized signal, and an absolute error between the slopes up to 0.2. Thus, we are able to find a layer containing the Rayleigh information, but following out inversion scheme we need to select just one reference Rayleigh point. The selection of this point inside the layer is done in the iterative procedure described below.
- Backward Klett inversion (Step 3): An iterative Klett inversion process is performed for 240 values of  $LR$  ranging from 35 to 150 Sr each 0.5 sr, and for all possible height reference points inside Rayleigh layer to retrieve  $\beta_p$  and  $\alpha_p$ . The goal with this iterative process is to run Klett until find a combination of  $LR$  and reference Rayleigh height that makes

comparable the integrated  $\alpha_p$  profile with the interpolated  $AOD_{910}$  from sun photometer at the same UTC time. The retrievals are considered as successful when the difference between integrated  $\alpha_p$  profile and  $AOD_{910}$  is lower than 0.001.

Once the signal is pre-processed, the explained Klett inversion is applied and the results are shown in Fig.5 for the case of 5 11<sup>th</sup> October 2019 at ONERA site. The molecular profile (black dotted line in Fig.5a) is calculated using Rayleigh theory fed with temperature and RH profiles from MWR. The cases presented here had a normalization range from 1.5 to 5 km, assuring a region where Rayleigh and  $RCS_w$  slopes are comparable. In Fig.5a the Rayleigh zone is detected from 1.8 to 3.0 km agl, and particularly in this example case an absolute slope error of 0.05 with  $r^2 = 0.9$  was found. The aim in the determination of the Rayleigh zone is to find the right altitude of reference to perform the backward Klett inversion.

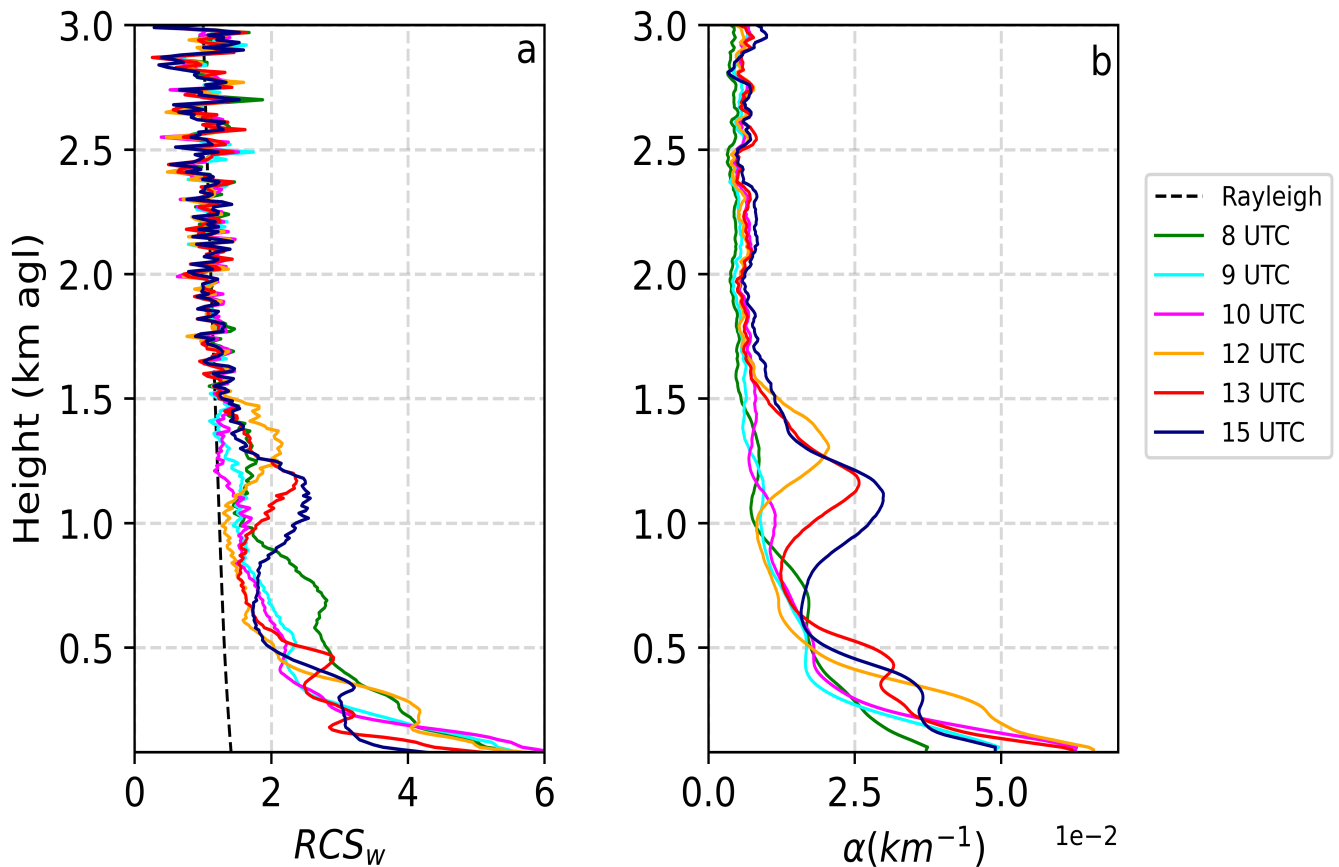


**Figure 5.** Example case of Klett inversion performed on 11<sup>th</sup> October 2019 for the time-frames that sun photometer has *LR* data availability. The  $AOD_{910}$  was interpolated from AERONET data at the same UTC time of the 1h-averaged  $RCS_w$ . The black dotted line in a) refers to the Rayleigh fit profile and in colors are presented in a) the  $RCS_w$  profiles used as input for the retrieval, while in b) is represented the  $\alpha_p$  resulting from the inversion

In order to assure the full overlap, it is used 250 m agl as the overlap height during the Klett inversion. The example case shown here present the evolution of the inversions since early morning until afternoon, but only shown those coincident with  $LR$  retrieval from sun photometer. The dynamic of the atmosphere started with the aerosol relatively compressed below the planetary boundary layer (PBL) (below 0.8 km agl) due to the lack of solar radiation, but after 10 UTC the layers started to mix along the atmospheric column showing two aerosol accumulations, from 0.4 to 0.5 km agl and from 1.0 to 1.2 km agl. According to AERONET, during the day we had the presence of mixed aerosols between urban and dust particles over Toulouse, predominating the coarse mode in the size distribution reaching  $0.019 \mu \text{ m}^3 / \mu \text{ m}^2$ . The iterative Klett procedure for having  $\beta_p$  profiles was performed by following the methodology, and then  $\alpha_p$  profiles were obtained as it is shown in Fig.5b. During the morning,  $\alpha_p$  was up to  $0.03 \text{ km}^{-1}$  in the first atmospheric layers (from 0.2 to 0.5 km agl), and then from 10 to 15 UTC  $\alpha_p$  reached up  $0.05 \text{ km}^{-1}$  below the first 0.5 km agl.  $\alpha_p=0.03 \text{ km}^{-1}$  for the pronounced aerosol peaks from 12 to 15 UTC.

One of the pursued parameters on lidar inversion is the  $LR$ , in our case, over Toulouse area there is no previous information about this parameter, therefore as one of the main goals for the application of a semi-automatic Klett is to have in the near future a relative robust data base that will help us to understand better the aerosol behaviour over the region and also to have more tools for retrieving aerosol optical properties. Table1 presents the  $LR$  obtained from Klett inversion, reporting an increasing  $LR$  along the day ranging from 58.1 to 99.0 sr, with a positive correlation with the AOD increase. In the early morning, the  $LR$  values found are comparable with those reported in Cazorla et al., 2017 and Marcos et al., 2018 for dust aerosols up to 60 Sr, but after 10 UTC the  $LR$  values obtained here increased up to 99 sr. In most of the studies, the  $LR$  is imposed for the klett calculation because of the previous knowledge of the aerosol type, but in our case  $LR$  is obtained from the continuous AOD cross-checking during the algorithm iterations, giving us the possibility to explore a wide range of  $LR$  values that are related with different aerosol types.

**Table 1.** Klett inversions on 11<sup>th</sup> October 2019. AERONET  $LR$  at 910 nm was considered as reference for absolute error calculation

UTC	AERONET AOD <sub>910</sub>	Klett AOD	Klett $LR$ (sr)	AERONET $LR_{910}$ (sr)	AbsErr(%)
8	0.038	0.039	72.2	65.9	9.6
9	0.044	0.045	58.1	62.4	6.9
10	0.051	0.052	68.7	72.2	4.8
12	0.058	0.059	83.6	58.1	43.9
13	0.059	0.060	99.0	68.7	44.1
15	0.060	0.061	87.9	66.6	32.0

As it was demonstrated in Dubovik et al., 2006 and Landulfo et al., 2008,  $LR$  can be obtained directly from sunphotometric measurements, thus following the same procedure, the absolute errors between AERONET  $LR$  and Klett  $LR$  were lower than 44 %, considering AERONET's  $LR$  as the reference (see Table1). The larger values found for  $LR$  with Klett inversion might be associated to the presence of the mixed aerosol (e.g. polluted dust), the physical separation between the sun photometer and the

ceilometer, and also due to instrumental parameters that increase the uncertainties (e.g lidar constant). The inversions left two open paths for future works, the first one is related to the calculation of the ceilometer calibration constant along the seasons to considering different scenarios, and the second is the design of the field campaigns for co-located measurements between ground base lidars and the ceilometer in order to inter-compare inversion products and improve the overlap information of the instrument.

## 5 Errors from water vapor uncertainties

The methodology applied to aerosol profiles retrieval needs from water vapor profiles, which in this work are obtained by MWR. But this water vapor information is not available in many stations with CL51 ceilometer. In order to use this method when MWR information is not available, atmospheric profiles from HYSPLIT model can be used, but it will add an extra uncertainty. This section is focused on quantify the uncertainties in the aerosol retrieval caused by the use of water vapor from HYSPLIT instead of MWR measurements. In this sense, two scenarios are considered: the first one by using 2 months (October-November 2019) of radiosounding profiles retrieved from HYSPLIT model, and the other one using measured profiles from the MWR, both at ONERA site.

### 5.1 HYSPLIT vs MWR data

In order to characterize the inversion calculation, a 2-step error estimation procedure is proposed (see Fig.1). In the first step, it was used a 2 months database (October-November 2019) from atmospheric measurements of temperature and AH from MWR, and modelled radiosondes retrieved using the GDAS meteorological database from HYSPLIT model. The aim is to estimate the root mean square error (RMSE) and mean bias error (MBE) between temperature, AH and  $N(r)_w$  profiles assuming MWR as the reference, evaluating the error between model and MWR atmospheric data.

Figure 6 presents the result of the two-months error comparison between HYSPLIT modelled radiosondes retrieved at ONERA location using the GDAS meteorological database and the MWR profiles. The data were chosen assuring coincidence of the temporal and spatial resolutions between soundings and MWR profiles from 0 to 10 km agl. For the analysis, 488 coincident cases were found. Temperature and AH, the main variables involved in the pre-processing and inversion, were evaluated.  $N_w$  was also analyzed but the RMSE and MBE errors were relatively lower and highly dependant of the temperature and AH errors. Figure 6ab shows in red line the temperature profiles of RMSE and MBE calculations, pointing out that below 2 km agl the RMSE reach the lowest values (lower than 4 °C), but after that altitude the RMSE increase monotonically until 6 °C. Therefore assuming the MWR as the reference, the results indicate that modelled radiosondes can be far from the MWR measurements at least 4 °C in the crucial zone for ceilometer profiles. The Fig.6b shows that temperature retrieved profiles from HYSPLIT are always sub-estimating the MWR ones, being critical around the first hundred meters agl. For AH profiles (blue lines, Fig.6ab), the RMSE shows values below 1.5 gm<sup>-3</sup> for the whole profile, however between 3.7 to 5.7 km agl, the RMSE presented a peak, which might be associated to the atmospheric region where the number of water vapor molecules



decrease with height drastically as it was also seen in Marcos et al., 2018. The MBE of the AH is quite variable, the ranges that overestimate the profile are from 0 to 200 m and 3 km to 5.8 km agl and the sub estimation ranges are from 1 km to 2.3 km and from 5.8 km to the end.

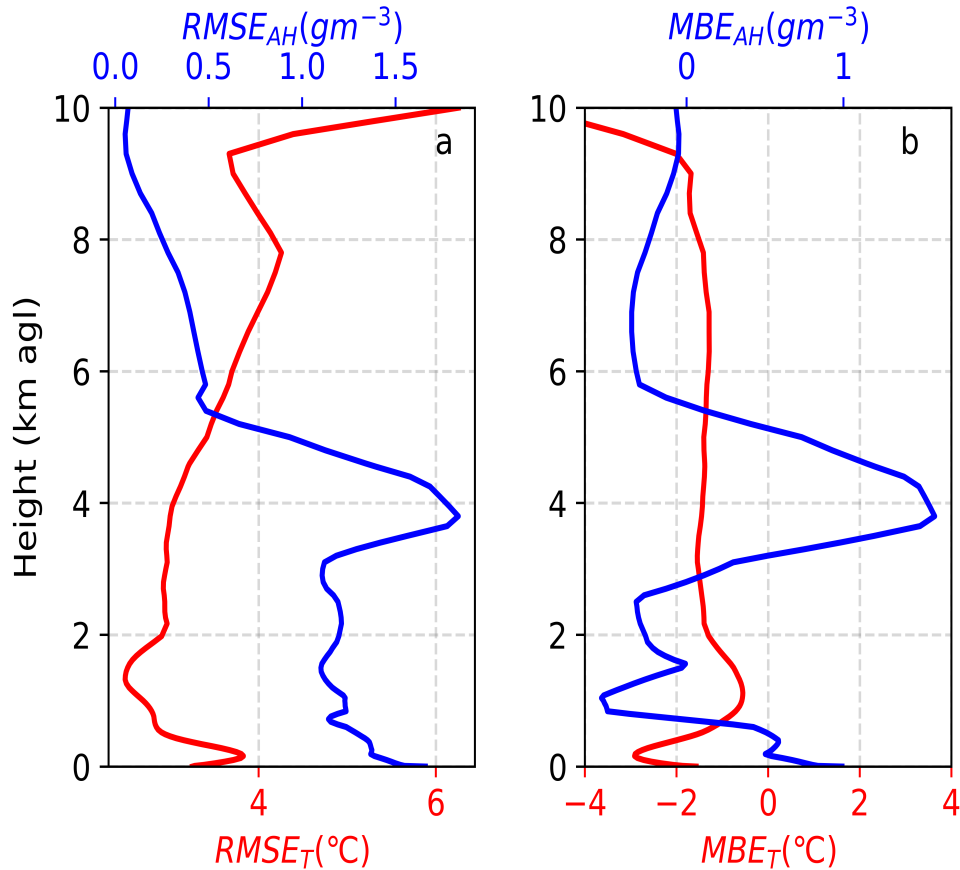


**Figure 6.** It is presented the error calculation in terms of RMSE and MBE, panel a) and b) respectively. For both panels, red line refers to temperature and blue line to AH.

## 5.2 Uncertainty propagation on aerosol profiles

- The second part of the error calculation is performed just to six particular cases where lidar inversion was applied. In the last section, it was seen the performance of the atmospheric variables between measured and modelled data, but here we centered our attention in determining the error propagation in terms of the absolute error (AbsE) for temperature, AH, RCS,  $\beta_p$  and  $\alpha_p$  in order to evaluate the total error during inversion process considering modelled data instead of atmospheric measurements.

In Fig.7 are presented the errors of the input measurements used for retrieving  $\beta_p$  and  $\alpha_p$  using the Klett inversion already discussed. In Fig.7a is reported the absolute error in percentage between temperature and AH profiles considering MWR as reference, from there it can be seen that absolute errors in temperature (red line) are higher in the first 800 m agl (up to 5 %), but then, the absolute error do not surpasses 1 %. Meanwhile, AH presented higher absolute errors. AH absolute errors (blue line) below 2 km agl were lower than 20 %, but above 2 km agl the errors can reach 100 % faster. The absolute errors on  $N_w$  at using the model or the MWR data are really lower, practically negligible (Fig.7b).

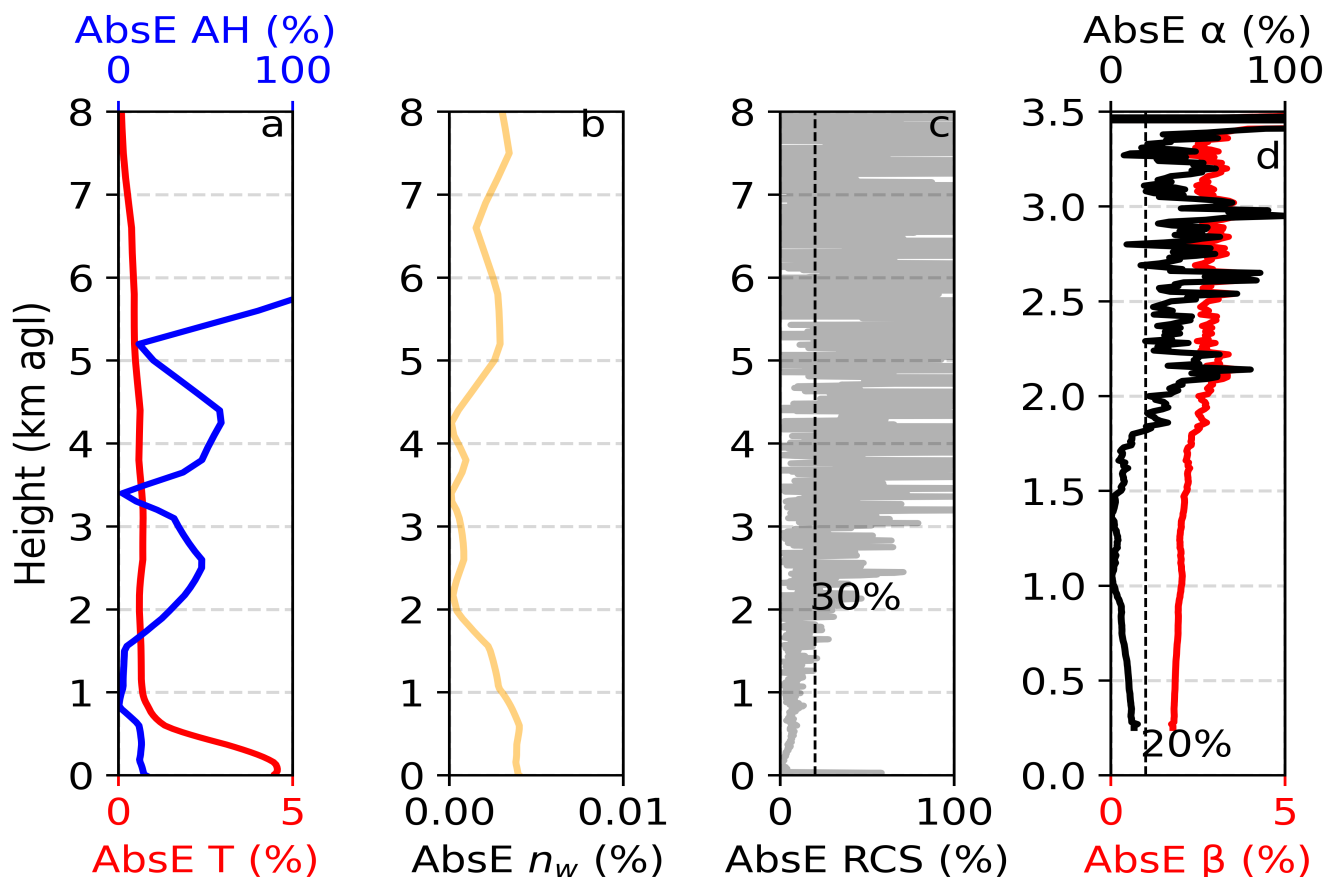


**Figure 7.** The panel presents the different steps in the example case on 11<sup>th</sup> October 2019 at 8 UTC for evaluation the absolute error (AbsE) in the inversion process. a) In red lines is represented the temperature and blue line refers to AH, b) is the  $N_w$ , c) is the error committed in the  $RCS_w$  signal, and d) AbsE of the  $\beta_p$  (red line), and  $\alpha_p$  (black line)

Figure7c shows the absolute error on the  $RCS_w$  profile for the same example case presented in sec. 4.2. Therefore, the results of having up to 1 % absolute error in temperature and close to 20 % in AH are causing an increase in the  $RCS_w$  absolute error up to 30 % below 2 km agl, and above this height the absolute error increase drastically reaching up more than 100 % above 3.5 km agl. The evaluation of this error in the Klett inversion is presented in Fig.7d (red line for  $\beta_p$  and

black line for  $\alpha_p$ ), where absolute errors in the first 2 km agl reached up to 3 % in  $\beta_p$ , and up to 20 % in  $\alpha_p$ . The errors in the  $RCS_w$  profile due to the use of modelled data instead measured can be seen in Fig.7c, however the errors reported in Fig.7d involve not only those ones from the  $RCS_w$ , but also those from the Klett inversion itself such as the accuracy at finding the molecular zone and  $LR$  selection, which depends highly on the external sources like sunphotometric measurements.

5

Table2 reports the mean values of the absolute error in percentage for six cases evaluated during the two-months study. The cases 1,2,3 were retrieved on 11<sup>th</sup> October 2019 at 06:00, 09:00, and 12:00 UTC, case 4 to 20<sup>th</sup> November 2019 at 06:00 UTC and cases 5 and 6 to 21<sup>st</sup> November 2019 at 09:00 and 12:00 UTC. The averages were calculated for 5 different layers: from 0 to 0.5 km agl, from 0.5 to 1 km agl, from 1 to 2 km agl, from 2 to 3 km agl and from 3 to 5 km agl. The inversion products ( $\beta_p$  and  $\alpha_p$ ) were analyzed until 2 km agl.

Table2 shows that mean temperature absolute errors were always below 4 % with lower standard deviation (SD). However, in the first 0.5km agl case 2 and 3 presented mean values up to 4 %. On the contrary, AH presented higher mean error values mainly above 3 km agl as it was expected from the analysis performed in the previous section with mean errors higher than 40 %.

Centering the attention in the first two kilometres of the atmosphere, the errors in AH were below 30 %, except for case 5,6 with mean errors up to 55 %. As it was seen on sec 3.2, the AH is deeply linked with the transmittance term for cleaning the  $RCS^*$  signal, therefore the relatively large differences in AH profiles are contributing to  $RCS_w$  final profiles. According to our results, mean absolute errors up to 30 % in AH might cause errors in  $RCS_w$  that reach 10 % in the first 2 km agl, and like the amount of water vapor is highly variable in the first two kilometers of the atmosphere, nearly-real measurements of AH will improve the ceilometer signal significantly, otherwise calculations without using real ambient measurements might lead to considerable error increase.

The retrieved products  $\beta_p$  and  $\alpha_p$  have an absolute error that is influenced firstly by the input data which are Rayleigh and  $RCS_w$  profiles, and secondly the good atmospheric reference to start the backward inversion, which is linked with the sunphotometric data for setting the correct  $LR$ , among other errors associated to the algorithm calculation itself. From Table2, is possible to see that in general, the mean absolute error is lower than 3 % below 2 km agl for  $\beta_p$ , meanwhile the errors in  $\alpha_p$  can reach 25 % within this height. Some mean errors for  $\alpha_p$  in cases 4,5,6 are quite larger than other cases, and this might be linked with the relative elevated AH errors (see on Table2). Considering this error propagation in  $\alpha_p$ , we found that without using co-located atmospheric measurements, this inversion product can be also estimated but considering an addition up to 12 % of absolute error for Vaisala CL51 ceilometers.

The high standard deviation errors reported for the  $RCS_w$  from 3 to 5 km agl (Table2) are associated to the increase of the noise that we already discussed in the pre-processing section, linked with the quality of the ceilometer signals and also in Fig.7c where the absolute error of the  $RCS_w$  increased considerably faster above 3 km agl, pointing out that aerosol inversion with ceilometers above 3 km agl might lead to larger errors.

**Table 2.** Mean absolute error calculated for six inversion cases using the semi-automatic Klett method. The variables evaluated were Temperature, AH,  $RCS_w$ ,  $\beta_p$  and  $\alpha_p$ . The study cases 1,2,3 were measured on 11<sup>th</sup> October 2019 at 6 h, 9 h, and 12 h respectively, case 4 on 20<sup>th</sup> November 2019 at 6 h and cases 5 and 6 on 21<sup>st</sup> November 2019 at 9 h and 12 h. The mean values are calculated for five different atmospheric volumes: from 0 to 0.5 km agl, from 0.5 to 1 km agl, from 1 to 2 km agl, from 2 to 3 km agl and from 3 to 5 km agl

		<b>0 to 0.5 km agl</b>	<b>0.5 to 1 km agl</b>	<b>1 to 2 km agl</b>	<b>2 to 3 km agl</b>	<b>3 to 5 km agl</b>
<b>T (%)</b>	<b>Case 1</b>	1,8 ± 0,9	0,1 ± 0,1	0,70 ± 0,08	0,92 ± 0,08	0,81 ± 0,07
	<b>Case 2</b>	3,9 ± 0,7	1,1 ± 0,3	0,65 ± 0,02	0,66 ± 0,04	0,63 ± 0,05
	<b>Case 3</b>	3,4 ± 0,4	2,5 ± 0,4	1,3 ± 0,2	1,00 ± 0,05	1,11 ± 0,06
	<b>Case 4</b>	1,5 ± 0,5	0,14 ± 0,08	0,5 ± 0,3	0,87 ± 0,03	0,82 ± 0,06
	<b>Case 5</b>	2,1 ± 0,7	0,3 ± 0,1	0,6 ± 0,2	0,72 ± 0,05	0,3 ± 0,2
	<b>Case 6</b>	2,0 ± 0,4	1,4 ± 0,3	0,88 ± 0,05	0,85 ± 0,04	0,7 ± 0,2
<b>AH(%)</b>	<b>Case 1</b>	10 ± 1	5 ± 3	12 ± 9	49 ± 4	37 ± 18
	<b>Case 2</b>	13,4 ± 0,9	6 ± 5	7 ± 7	43 ± 4	37 ± 18
	<b>Case 3</b>	16,5 ± 0,7	11 ± 4	6 ± 4	34 ± 4	41 ± 21
	<b>Case 4</b>	3 ± 1	6 ± 4	25 ± 13	76 ± 5	39 ± 16
	<b>Case 5</b>	3 ± 1	18 ± 9	53 ± 17	86 ± 12	42 ± 18
	<b>Case 6</b>	3 ± 2	20 ± 9	55 ± 17	85 ± 13	43 ± 18
$RCS_w$ (%)	<b>Case 1</b>	4 ± 10	5 ± 2	8 ± 6	23 ± 19	28 ± 603
	<b>Case 2</b>	5 ± 9	5 ± 2	8 ± 6	20 ± 15	86 ± 1967
	<b>Case 3</b>	5 ± 5	5 ± 2	9 ± 7	22 ± 18	60 ± 314
	<b>Case 4</b>	2 ± 3	5 ± 3	7 ± 6	20 ± 18	16 ± 646
	<b>Case 5</b>	3 ± 4	3 ± 2	7 ± 6	16 ± 15	57 ± 263
	<b>Case 6</b>	5 ± 9	3 ± 2	8 ± 7	24 ± 24	49 ± 676
$\beta_p$ (%)	<b>Case 1</b>	1,81 ± 0,02	1,92 ± 0,04	2,2 ± 0,3		
	<b>Case 2</b>	1,77 ± 0,03	1,69 ± 0,02	1,62 ± 0,04		
	<b>Case 3</b>	1,67 ± 0,01	1,18 ± 0,02	1,18 ± 0,05		
	<b>Case 4</b>	0,85 ± 0,02	0,88 ± 0,03	0,46 ± 0,08		
	<b>Case 5</b>	1,26 ± 0,02	1,23 ± 0,07	1,1 ± 0,2		
	<b>Case 6</b>	0,96 ± 0,02	0,7 ± 0,2	0,20 ± 0,07		
$\alpha_p$ (%)	<b>Case 1</b>	12 ± 1	7 ± 2	10 ± 11		
	<b>Case 2</b>	5 ± 1	0,7 ± 0,6	4 ± 2		
	<b>Case 3</b>	1,5 ± 0,7	2 ± 1	3 ± 2		
	<b>Case 4</b>	3 ± 2	7 ± 3	44 ± 10		
	<b>Case 5</b>	1,3 ± 0,8	4 ± 4	18 ± 10		
	<b>Case 6</b>	26 ± 3	25 ± 20	73 ± 9		

## 6 Conclusions

The purpose of this work is to tackle the central problems that Vaisala CL51 ceilometers have for improving aerosol inversion products. Firstly, the ceilometer pre-processing is discussed by taking advantage of the termination hood external tool. Between day and night the instrument presented only small differences in terms of shape and noise levels of DC signals detected, therefore we decided to work with 30 min-averaged night-time DC profiles. For the BG analysis, we used a systematic selection of the best BG region, avoiding that  $RCS^*$  goes to negative values within the first 5 km agl. After suppressing DC and BG, the signal remained positive far than 5 km agl and S-shape oscillations were minimized.

The methodology designed involved the water vapor correction by using a co-located MWR for measuring atmospheric variables. This synergy allowed us to improve the quality of the signal by calculating the water vapor transmission term of the lidar equation using real measurements of temperature and AH, and deriving from them the  $N_w$ . For the inversion, Rayleigh profiles were calculated using MWR measurements and the  $RCS_w$  profiles. In addition,  $AOD_{910}$  data from the sunphotometer were used for finding the best  $\beta_p$  profile, integrating the  $\alpha_p$  profile for different  $LR$  until the minimum difference ( $\leq 0.001$ ) with the  $AOD_{910}$  is found.

15

The error estimation was performed first by means of the RMSE and MBE estimators calculated for two-months of temperature and AH modelled HYSPLIT radiosondes and MWR. The main objective was to set an error estimation for the main two atmospheric variables involved in the  $RCS_{raw}$  profiles correction, and those ones that are playing a crucial role in the inversion process. The errors were calculated for 488 samples covering different atmospheric scenarios, showing that for temperature below 2km agl the RMSE is lower than 4 °C, and above is up to 6 °C, whereas AH presented an error up to 2 gm<sup>-3</sup>, which in terms of water vapor correction can be significant. The MBE shown that temperature modelled profiles were always sub estimating MWR ones (up to -1 °C), and AH MBE was high variable, underestimating the MWR measures from 1 km to 2.3 km agl and from 5.8 km agl to the end of the profile (reaching up -0.5 gm<sup>-3</sup>) and the overestimation reached up 1.5 gm<sup>-3</sup> from ground to 0.2 km agl and from 3 km to 5.8 km agl.

25

In summary, we found that the use of modelled data instead atmospheric measurements is primarily influencing the  $RCS_w$ , and then the inversion products obtained from the ceilometer. As a result of that, the absolute error estimation within the critical zone for aerosol inversion (first 2km agl), the temperature presented errors below 4%, while in the first 3 km agl AH were below 25 %. These errors affected the  $RCS_w$  signal driving to an error up to 9 % in the first 3km agl. The errors in  $\beta_p$  during Klett calculation were lower than 2.2 %, leading to an error in  $\alpha_p$  up to 25 %.

30

Finally, the Klett algorithm could be improved by determining the calibration constant of the instrument tackling one of the E-PROFILE aims. This work can be developed in further studies by having a larger ceilometer database for making a seasonal analysis of the calibration constant as function of the internal temperature in a semi-automatic way at ONERA site. In addition,

the knowledge of the full overlap height of the system could also help us to improve the inversion products, therefore a further measurement campaign with ground based lidar operating co-located to the ceilometer might be an ideal solution to have the ceilometer fully characterized.

#### *Author contributions.*

- 5     Andrés E. Bedoya-Velásquez and Marcos Herreras processed the data. Andrés Esteban Bedoya-Velásquez and Marcos Herreras designed the methodology, and ran the codes. Andrés Esteban Bedoya-Velásquez wrote the manuscript with contributions from all coauthors. Sidonie Lefbvre : supervision; Matthias Wiegner and Thierry Huet : investigation; Romain Ceolato : supervision, conceptualization, and review.

- Acknowledgements.* The authors gratefully acknowledge funding from ONERA (PROMETE project). We thank Alain Dabas for its effort in  
10    establishing and maintaining the AERONET Toulouse *MF* site.

#### **References**

- Boucher, O., Randall, D., Artaxo, P., Bretherton, C., Feingold, G., Forster, P., Kerminen, V.-M., Kondo, Y., Liao, H., Lohmann, U., Rasch, P., Satheesh, S. K., Sherwood, S., Stevens, B., & Zhang, X. Y. (2013). Clouds and aerosols. In T. F. Stocker, D. Qin, G.-K. Plattner, M. Tignor, S. K. Allen, J. Doschung, A. Nauels, Y. Xia, V. Bex, & P. M. Midgley (Eds.), *Climate change 2013: The physical science basis. contribution of working group i to the fifth assessment report of the intergovernmental panel on climate change* (pp. 571–657). Cambridge, UK, Cambridge University Press. <https://doi.org/10.1017/CBO9781107415324.016>
- 15     Chaikovsky, A., Dubovik, O., Holben, B., Bril, A., Goloub, P., Tanré, D., Pappalardo, G., Wandinger, U., Chaikovskaya, L., Denisov, S., Grudo, J., Lopatin, A., Karol, Y., Lapyonok, T., Amiridis, V., Ansmann, A., Apituley, A., Allados-Arboledas, L., Binietoglou, I., ... Wang, X. (2016). Lidar-radiometer inversion code (liric) for the retrieval of vertical aerosol properties from combined  
20     lidar/radiometer data: Development and distribution in earlinet. *Atmospheric Measurement Techniques*, 9(3), 1181–1205. <https://doi.org/10.5194/amt-9-1181-2016>
- Lopatin, A., Dubovik, O., Chaikovsky, A., Goloub, P., Lapyonok, T., Tanré, D., & Litvinov, P. (2013). Enhancement of aerosol characterization using synergy of lidar and sun-photometer coincident observations: The garrlic algorithm. *Atmospheric Measurement Techniques*, 6(8), 2065–2088. <https://doi.org/10.5194/amt-6-2065-2013>
- 25     Benavent-Oltra, J. A., Román, R., Granados-Muñoz, M. J., Pérez-Ramírez, D., Ortiz-Amezcu, P., Denjean, C., Lopatin, A., Lyamani, H., Torres, B., Guerrero-Rascado, J. L., Fuertes, D., Dubovik, O., Chaikovsky, A., Olmo, F. J., Mallet, M., & Alados-Arboledas, L. (2017). Comparative assessment of grasp algorithm for a dust event over granada (spain) during charmex-adrimed 2013 campaign. *Atmospheric Measurement Techniques*, 10(11), 4439–4457. <https://doi.org/10.5194/amt-10-4439-2017>
- Benavent-Oltra, J. A., Román, R., Casquero-Vera, J. A., Pérez-Ramírez, D., Lyamani, H., Ortiz-Amezcu, P., Bedoya-Velásquez, A. E., de  
30     Arruda Moreira, G., Barreto, A., Lopatin, A., Fuertes, D., Herrera, M., Torres, B., Dubovik, O., Guerrero-Rascado, J. L., Goloub,

- P., Olmo-Reyes, F. J., & Alados-Arboledas, L. (2019). Different strategies to retrieve aerosol properties at night-time with the grasp algorithm. *Atmospheric Chemistry and Physics*, *19*(22), 14149–14171. <https://doi.org/10.5194/acp-19-14149-2019>
- 5 Bedoya-Velásquez, A. E., Navas-Guzmán, F., Granados-Muñoz, M. J., Titos, G., Román, R., Casquero-Vera, J. A., Ortiz-Amezcuca, P., Benavent-Oltra, J. A., de Arruda Moreira, G., Montilla-Rosero, E., Hoyos, C. D., Artiñano, B., Coz, E., Olmo-Reyes, F. J., Alados-Arboledas, L., & Guerrero-Rascado, J. L. (2018). Hygroscopic growth study in the framework of earlinet during the slope i campaign: Synergy of remote sensing and in situ instrumentation. *Atmospheric Chemistry and Physics*, *18*(10), 7001–7017. <https://doi.org/10.5194/acp-18-7001-2018>
- 10 de Arruda Moreira, G., Guerrero-Rascado, J. L., Benavent-Oltra, J. A., Ortiz-Amezcuca, P., Román, R., E. Bedoya-Velásquez, A., Bravo-Aranda, J. A., Olmo Reyes, F. J., Landulfo, E., & Alados-Arboledas, L. (2019). Analyzing the turbulent planetary boundary layer by remote sensing systems: The doppler wind lidar, aerosol elastic lidar and microwave radiometer. *Atmospheric Chemistry and Physics*, *19*(2), 1263–1280. <https://doi.org/10.5194/acp-19-1263-2019>
- 15 Bedoya-Velásquez, A. E., Titos, G., Bravo-Aranda, J. A., Haeffelin, M., Favez, O., Petit, J.-E., Casquero-Vera, J. A., Olmo-Reyes, F. J., Montilla-Rosero, E., Hoyos, C. D., Alados-Arboledas, L., & Guerrero-Rascado, J. L. (2019). Long-term aerosol optical hygroscopicity study at the actris sirta observatory: Synergy between ceilometer and in situ measurements. *Atmospheric Chemistry and Physics*, *19*(11), 7883–7896. <https://doi.org/10.5194/acp-19-7883-2019>
- Haeffelin, M., Laffineur, Q., Bravo-Aranda, J.-A., Drouin, M.-A., Casquero-Vera, J.-A., Dupont, J.-C., & De Backer, H. (2016). Radiation fog formation alerts using attenuated backscatter power from automatic lidars and ceilometers. *Atmospheric Measurement Techniques*, *9*(11), 5347–5365. <https://doi.org/10.5194/amt-9-5347-2016>
- 20 Wiegner, M., Madonna, F., Biniotoglou, I., Forkel, R., Gasteiger, J., Geiß, A., Pappalardo, G., Schäfer, K., & Thomas, W. (2014). What is the benefit of ceilometers for aerosol remote sensing? an answer from earlinet. *Atmospheric Measurement Techniques*, *7*(7), 1979–1997. <https://doi.org/10.5194/amt-7-1979-2014>
- Jin, Y., Kai, K., Kawai, K., Nagai, T., Sakai, T., Yamazaki, A., Uchiyama, A., Batdorj, D., Sugimoto, N., & Nishizawa, T. (2015). Ceilometer calibration for retrieval of aerosol optical properties [Topical issue on optical particle characterization and remote sensing of the atmosphere: Part II]. *Journal of Quantitative Spectroscopy and Radiative Transfer*, *153*, 49–56. <https://doi.org/10.1016/j.jqsrt.2014.10.009>
- 25 Cazorla, A., Casquero-Vera, J. A., Román, R., Guerrero-Rascado, J. L., Toledano, C., Cachorro, V. E., Orza, J. A. G., Cancillo, M. L., Serrano, A., Titos, G., Pandolfi, M., Alastuey, A., Hanrieder, N., & Alados-Arboledas, L. (2017). Near-real-time processing of a ceilometer network assisted with sun-photometer data: Monitoring a dust outbreak over the iberian peninsula. *Atmospheric Chemistry and Physics*, *17*(19), 11861–11876. <https://doi.org/10.5194/acp-17-11861-2017>
- 30 Román, R., Benavent-Oltra, J., Casquero-Vera, J., Lopatin, A., Cazorla, A., Lyamani, H., Denjean, C., Fuertes, D., Pérez-Ramírez, D., Torres, B., Toledano, C., Dubovik, O., Cachorro, V., [de Frutos], A., Olmo, F., & Alados-Arboledas, L. (2018). Retrieval of aerosol profiles combining sunphotometer and ceilometer measurements in grasp code. *Atmospheric Research*, *204*, 161–177. <https://doi.org/10.1016/j.atmosres.2018.01.021>
- 35 Herreras, M., Román, R., Cazorla, A., Toledano, C., Lyamani, H., Torres, B., Cachorro, V. E., Olmo, F. J., Alados-Arboledas, L., & de Frutos, Á. M. (2018). Integrated aerosol extinction profiles from ceilometer and sunphotometer combination against sunphotometer measurements at various heights. *IGARSS 2018 - 2018 IEEE International Geoscience and Remote Sensing Symposium*, 7564–7567.

- Titos, G., Ealo, M., Román, R., Cazorla, A., Sola, Y., Dubovik, O., Alastuey, A., & Pandolfi, M. (2019). Retrieval of aerosol properties from ceilometer and photometer measurements: Long-term evaluation with in situ data and statistical analysis at montsec (southern pyrenees). *Atmospheric Measurement Techniques*, 12(6), 3255–3267. <https://doi.org/10.5194/amt-12-3255-2019>
- 5 Kotthaus, S., O'Connor, E., Munkel, C., Charlton-Perez, C., Haeffelin, M., Gabey, A. M., & Grimmond, C. S. B. (2016). Recommendations for processing atmospheric attenuated backscatter profiles from vaisala cl31 ceilometers. *Atmospheric Measurement Techniques*, 9(8), 3769–3791. <https://doi.org/10.5194/amt-9-3769-2016>
- Marcos, C. R., Gómez-Amo, J. L., Peris, C., Pedrós, R., Utrillas, M. P., & Martínez-Lozano, J. A. (2018). Analysis of four years of ceilometer-derived aerosol backscatter profiles in a coastal site of the western mediterranean. *Atmospheric Research*, 213, 331–345. <https://doi.org/10.1016/j.atmosres.2018.06.016>
- 10 Wiegner, M., & Gasteiger, J. (2015). Correction of water vapor absorption for aerosol remote sensing with ceilometers. *Atmospheric Measurement Techniques*, 8(9), 3971–3984. <https://doi.org/10.5194/amt-8-3971-2015>
- Klett, J. D. (1985). Lidar inversion with variable backscatter/extinction ratios. *Appl. Opt.*, 24(11), 1638–1643. <https://doi.org/10.1364/AO.24.001638>
- Klett, J. D. (1981). Stable analytical inversion solution for processing lidar returns. *Appl. Opt.*, 20(2), 211–220. <https://doi.org/10.1364/AO.20.000211>
- 15 Rose, T., Crewell, S., Löhnert, U., & Simmer, C. (2005). A network suitable microwave radiometer for operational monitoring of the cloudy atmosphere [CLIWA-NET: Observation and Modelling of Liquid Water Clouds]. *Atmospheric Research*, 75(3), 183–200. <https://doi.org/10.1016/j.atmosres.2004.12.005>
- Bedoya-Velásquez, A. E., Navas-Guzmán, F., de Arruda Moreira, G., Román, R., Cazorla, A., Ortiz-Amezcu, P., Benavent-Oltra, J. A., Alados-Arboledas, L., Olmo-Reyes, F. J., Foyo-Moreno, I., Montilla-Rosero, E., Hoyos, C. D., & Guerrero-Rascado, J. L. (2019). Seasonal analysis of the atmosphere during five years by using microwave radiometry over a mid-latitude site. *Atmospheric Research*, 218, 78–89. <https://doi.org/10.1016/j.atmosres.2018.11.014>
- 20 Holben, B., Eck, T., Slutsker, I., Tanré, D., Buis, J., Setzer, A., Vermote, E., Reagan, J., Kaufman, Y., Nakajima, T., Lavenu, F., Jankowiak, I., & Smirnov, A. (1998). Aeronet—a federated instrument network and data archive for aerosol characterization. *Remote Sensing of Environment*, 66(1), 1–16. [https://doi.org/10.1016/S0034-4257\(98\)00031-5](https://doi.org/10.1016/S0034-4257(98)00031-5)
- 25 Dubovik, O., & King, M. D. (2000). A flexible inversion algorithm for retrieval of aerosol optical properties from sun and sky radiance measurements. *Journal of Geophysical Research: Atmospheres*, 105(D16), <https://agupubs.onlinelibrary.wiley.com/doi/pdf/10.1029/2000JD900282>, 20673–20696. <https://doi.org/10.1029/2000JD900282>
- Dubovik, O., Holben, B., Eck, T. F., Smirnov, A., Kaufman, Y. J., King, M. D., Tanré, D., & Slutsker, I. (2002). Variability of absorption and optical properties of key aerosol types observed in worldwide locations. *Journal of the Atmospheric Sciences*, 59(3), [https://doi.org/10.1175/1520-0469\(2002\)059<0590:VOAOP>2.0.CO;2](https://doi.org/10.1175/1520-0469(2002)059<0590:VOAOP>2.0.CO;2), 590–608. [https://doi.org/10.1175/1520-0469\(2002\)059<0590:VOAOP>2.0.CO;2](https://doi.org/10.1175/1520-0469(2002)059<0590:VOAOP>2.0.CO;2)
- 30 Dubovik, O., Sinyuk, A., Lapyonok, T., Holben, B. N., Mishchenko, M., Yang, P., Eck, T. F., Volten, H., Muñoz, O., Veihelmann, B., van der Zande, W. J., Leon, J.-F., Sorokin, M., & Slutsker, I. (2006). Application of spheroid models to account for aerosol particle non-sphericity in remote sensing of desert dust. *Journal of Geophysical Research: Atmospheres*, 111(D11), <https://agupubs.onlinelibrary.wiley.com/doi/10.1029/2005JD006619>
- 35 Giles, D. M., Sinyuk, A., Sorokin, M. G., Schafer, J. S., Smirnov, A., Slutsker, I., Eck, T. F., Holben, B. N., Lewis, J. R., Campbell, J. R., Welton, E. J., Korkin, S. V., & Lyapustin, A. I. (2019). Advancements in the aerosol robotic network (aeronet) version 3 database –



automated near-real-time quality control algorithm with improved cloud screening for sun photometer aerosol optical depth (aod) measurements. *Atmospheric Measurement Techniques*, 12(1), 169–209. <https://doi.org/10.5194/amt-12-169-2019>

Stein, A. F., Draxler, R. R., Rolph, G. D., Stunder, B. J. B., Cohen, M. D., & Ngan, F. (2015). Noaa’s hysplit atmospheric transport and dispersion modeling system. *Bulletin of the American Meteorological Society*, 96(12), <https://doi.org/10.1175/BAMS-D-14-00110.1>, 2059–2077. <https://doi.org/10.1175/BAMS-D-14-00110.1>

5

Landulfo, E., Papayannis, A., Torres, A. S., Uehara, S. T., Pozzetti, L. M. V., Alencar de Matos, C., Sawamura, P., Morinobu Nakaema, W., & de Jesus, W. (2008). A four-year lidar–sun photometer aerosol study at são paulo, brazil. *Journal of Atmospheric and Oceanic Technology*, 25(8), <https://doi.org/10.1175/2007JTECHA984.1>, 1463–1468. <https://doi.org/10.1175/2007JTECHA984.1>